Near room temperature antiferromagnetic ordering with a potential low-dimensional magnetism in AlMn$_2$B$_2$

Tej N. Lamichhane,[1,*] Khusboo Rana,[1] Qisheng Lin,[2] Sergey L. Bud'ko,[1] Yuji Furukawa,[1] and Paul C. Canfield[1]

[1]*Ames Laboratory, U.S. DOE, and Department of Physics and Astronomy, Iowa State University, Ames, Iowa 50011, USA*
[2]*Ames Laboratory, U.S. DOE and Department of Chemistry, Iowa State University, Ames, Iowa 50011, USA*

We present self flux growth and characterization of single crystalline AlMn$_2$B$_2$. It is an orthorhombic (space group *Cmmm*), layered material with a platelike morphology. The anisotropic bulk magnetization data, electrical transport, and ^{11}B nuclear magnetic resonance (NMR) data revealed an antiferromagnetic (AFM) transition at 313 ± 2 K. In the magnetization data, there is also a broad local maximum significantly above the AFM transition that could be a signature of low-dimensional magnetic interactions in AlMn$_2$B$_2$.

I. INTRODUCTION

The AlT$_2$B$_2$ (T = Fe, Cr, Mn) system crystallizes in the orthorhombic, *Cmmm* structure and adopts a layer morphology with an internal structure of alternate stacking of Al atom planes and T$_2$B$_2$ slabs along the *b* axis [1]. A representative unit cell of AlMn$_2$B$_2$ is shown in Fig. 1(a) to demonstrate this atomic structure. AlT$_2$B$_2$ compounds are interesting, especially for potential rare earth free magnetocaloric materials and soft magnetic materials. AlFe$_2$B$_2$ is ferromagnetic and studied for its magnetocaloric and anisotropic magnetic properties [2–4]. Understanding the magnetic properties of the neighboring, isostructural compounds can provide further insight into the series as well as how to tune the magnetocaloric property of the AlFe$_2$B$_2$ via substitution. We started this work to clarify the magnetic properties of AlMn$_2$B$_2$ since it was identified as a nonmagnetic material [5]. In addition, some inconsistencies between bulk and local probe magnetic measurements in the Al(Fe$_{1-x}$Mn$_x$)$_2$B$_2$ were observed. A later first principle calculation suggested that AlMn$_2$B$_2$ should be an antiferromagnetic compound [6]. In a recent powder neutron study, AlMn$_2$B$_2$ is identified as a ceramic AFM compound [7] with Neel temperature around 390 K. A study of lattice parameters variation from room temperature to 1200 K revealed that there is a change in anisotropy nature in *a* and *c* lattice parameters around 450 K and a local minimum in *b* lattice parameters around 400 K [8]. The lack of a clear description of the nature or number of magnetic phase transitions in AlMn$_2$B$_2$ led us to grow and systematically study single crystalline samples.

This paper reports the synthesis of bulk single crystals via high-temperature solution growth and their characterization via high and low temperature magnetization, NMR, and electrical resistance measurements. We find that AlMn$_2$B$_2$ is a metallic antiferromagnet with a transition temperature of $T_N = 313 \pm 2$ K. In addition we find that AlMn$_2$B$_2$ has features associated with pseudo-two-dimensional magnets.

II. EXPERIMENTAL DETAILS

A. Crystal growth

Solution growth is a powerful tool even for compounds with high melting elements like B [3,9,10]. The major difficulty associated with solution growth is finding an initial composition that allows for growth of the single phase, desired compound. For example, CaKFe$_4$As$_4$ growth in single phase form presents an illustrative example [11]. Fortunately, with the innovation of fritted alumina crucibles sets [12] we can now reuse decanted melt and essentially fractionate the melt, as described below.

Al shot (Alfa Aesar 99.999%), B pieces (Alfa Aesar 99.5% metal basis), and Mn pieces (Alfa Aesar 99.9% metal basis) after surface oxidation cleaning as described elsewhere [13] were used for the crystal growth process. We started with an Al rich composition, Al$_{68}$Mn$_{22}$B$_{10}$, and arc-melted it at least four times under an Ar atmosphere. The button was then cut with a metal cutter and re-arcmelted if some not-reacted B pieces were found. After the button appeared to be homogeneous, it was packed in a fritted alumina crucible set [12] and sealed under partial pressure of argon inside an amorphous silica jacket to form a growth ampoule. The growth ampoule was then heated to 1200 °C over 2 h and soaked there for 10 h before spinning using a centrifuge. Due to a high melting point of B containing compounds, homogeneous liquid was not formed at 1200 °C. Undissolved polycrystalline MnB and Al-Mn binary compounds were separated at 1200 °C via centrifuging. The catch crucible collected the homogeneous melt at 1200 °C was again sealed in a fritted alumina crucible sets under Ar atmosphere to form second growth ampoule. This second ampoule was heated to 1200 °C over 2 h, held there for another 10 h and cooled down to 1100 °C over 50 h and spun using a centrifuge to separate the crystals. The
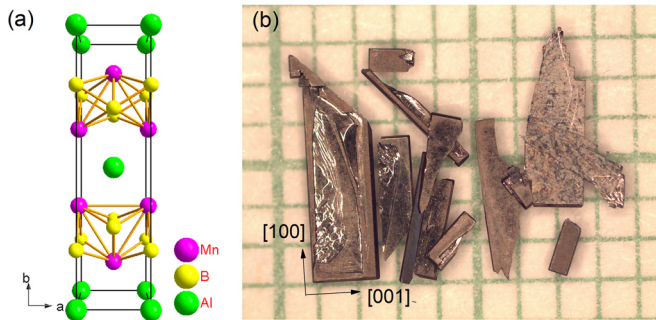
*Corresponding author: tejl@iastate.edu

FIG. 1. (a)$AlMn_2B_2$ unit cell showing Mn_2B_2 slabs stacked with Al layer. (b) Concentrated NaOH etched $AlMn_2B_2$ single crystals.

second growth attempt produced a mixture of the targeted $AlMn_2B_2$ phase along with MnB crystals. So as to avoid this MnB contamination, the catch crucible of the second growth was used for a third growth and sealed again under a partial pressure of Ar. For this stage, to make sure there are no other nucleated crystals, the third growth growth was heated to $1200\,^\circ$C over 2 h and soaked there for 2 h. It was then cooled down to $1100\,^\circ$C over 1 h and stayed there for 1 h followed by slow cooling to $990\,^\circ$C over 120 h and centrifuged to separate large, single phased $AlMn_2B_2$ crystals as shown in Fig. 1(b). The flux on the surface was removed via concentrated NaOH etching. It should be noted that predominantly single phase $AlMn_2B_2$ crystals were grown in single growth attempt using initial $Al_{84}Mn_8B_8$ composition however the crystals were small, due to multiple nucleation sites.

III. CRYSTAL STRUCTURE AND STOICHIOMETRY

As grown single crystals were characterized using a scanning electron microscope (SEM), as well as both powder and single crystal x-ray diffraction (XRD). Figures 2(a) and 2(b) show the planar and cross sectional backscattered SEM images of $AlMn_2B_2$ single crystals which show predominantly homogeneous compositions. The small linear grooves are the cracked layers associated with the SEM sample polishing. Being a layered material, it can be easily cleaved and deformed. Boron is difficult to account for correctly in electron dispersive spectroscopy(EDS), as a consequence of this we determined only the Mn:Al ratio for two different batches of single crystalline samples. In the first batch, 13 spots were analyzed in EDS with Mn:Al ratio of 2.07 for all characteristics x-ray emissions. Similarly, an eight spot analysis in the second batch provided the Mn:Al ratio to be 2.12 for characteristics K lines for all elements. With the L-characteristics-lines analysis, a ratio of 2.51 was obtained for the second batch. Without the creation and use of Mn-Al-B based standards, further characterization by EDS is difficult.

Although the EDS results are qualitatively in agreement with the $AlMn_2B_2$ structure, to more precisely determine the composition and structure, multiple batches of $AlMn_2B_2$ were investigated using single crystal XRD technique. Single crystalline XRD data were collected with the use of graphite monochromatized Mo K_α radiation ($\lambda = 0.71073$ Å) at room temperature on a Bruker APEX2 diffractometer. Reflections were gathered by taking five sets of 440 frames with 0.5°
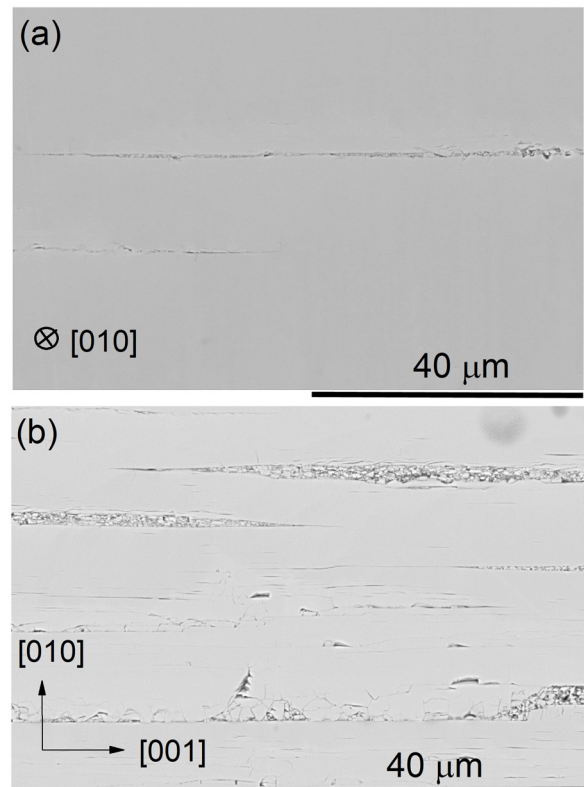

FIG. 2. (a) SEM image of $AlMn_2B_2$ single crystalline sample along the planar view (with electron beam parallel to [010]) (b) SEM image of $AlMn_2B_2$ in a cross sectional view with electron beam parallel to [100].

scans in ω/θ, with an exposure time of 10 s per frame and the crystal-to-detector distance of 6 cm. The structure solution and refinement for single crystal data was carried out using SHELXTL program package [14]. Attempts to refine occupancies of each site indicated full occupancy ($<3\sigma$). The final stage of refinement was performed using anisotropic displacement parameters for all the atoms. The refinement metrics and atomic coordinates are presented in Tables I and II, respectively. The single crystalline refinement showed $AlMn_2B_2$ as a stoichiometric material.

Etched single crystals were finely ground and spread over a zero background silicon wafer sample holder with the help of a thin film of Dow Corning high vacuum grease. Powder diffraction data were obtained using a Rigaku Miniflex II diffractometer within a 2θ range of 10–100° with a step of 0.02° and dwelling time of three seconds for data acquisition. The crystallographic information file from the single crystal XRD solution was used to fit the powder XRD data using GSAS [15] and EXPGUI [16] software packages. Figure 3 shows the Rietveld refined powder XRD pattern with R factor of 0.08. Being a relatively hard, layered material, texture is visible along the [020] direction although March Dollase texture correction was employed to account for this intensity mismatch.

To identify the crystallographic orientation of the $AlMn_2B_2$ single crystals, we employed the monochromatic x-ray diffraction from the crystallographic surfaces in the

TABLE I. Crystal data and structure refinement for $AlMn_2B_2$.

|	
Empirical formula	$AlMn_2B_2$
Formula weight	158.48
Temperature	296(2) K
Wavelength	0.71073 Å
Crystal system, space group	Orthorhombic, *Cmmm*
Unit cell dimensions	$a = 2.9215(1)$ Å
	$b = 11.0709(6)$ Å
	$c = 2.8972(2)$ Å
Volume	$93.706(9) \ 10^3$ Å^3
Z, Calculated density	2, 5.63 g/cm^3
Absorption coefficient	6.704 mm^{-1}
F(000)	73
θ range (°)	3.693 to 29.003
Limiting indices	$-5 \leqslant h \leqslant 5$
	$-22 \leqslant k \leqslant 22$
	$-5 \leqslant l \leqslant 5$
Reflections collected	1467
Independent reflections	270 [R(int) = 0.0401]
Completeness to theta = 25.242°	98.5%
Absorption correction	multiscan, empirical
Refinement method	Full-matrix least squares
Data/restraints/parameters	270 / 0 / 12
Goodness-of-fit on F^2	1.101
Final R indices [I > 2σ(I)]	$R1 = 0.0362$, $wR2 = 0.0817$
R indices (all data)	$R1 = 0.0387$, $wR2 = 0.0824$
Largest diff. peak and hole	2.341 and -1.249 e.Å^{-3}

Bragg-Brentano geometry [3,17]. The direction perpendicular to the plate was identified to be [010] since a family of {020} lines were observed in the diffraction pattern as shown in blue curve in Fig. 4. The plate was held vertical and the family of {001} peaks were obtained as shown in the red curve of Fig. 4. The monochromatic x-ray surface diffraction peaks were compared with powder diffraction data to correctly identify their directions. A vertical line through the powder [110] peak was used as a reference point of comparison as shown in Fig. 4. Then the last remaining direction was identified to be [100] along the length of the crystals. A reference coordinate system is shown in Fig. 1(b) to demonstrate the crystallographic orientations of $AlMn_2B_2$ crystals.

## IV. ELECTRIC AND MAGNETIC PROPERTIES

The temperature dependent electrical resistance of $AlMn_2B_2$ was measured in a traditional four probe measurement on a NaOH etched, rodlike sample using an external device control option to interface with a Linear

TABLE II. Atomic coordinates and equivalent isotropic displacement parameters (A^2) for $AlMn_2B_2$. U(eq) is defined as one third of the trace of the orthogonalized U_{ij} tensor.

atom	Wyckoff site	x	y	z	U_{eq}
Mn	4*j*	0	0.3552(1)	1/2	0.0070(1)
Al	2*a*	0	0	0	0.0067(5)
B	4*i*	0	0.2065(5)	0	0.0070(1)
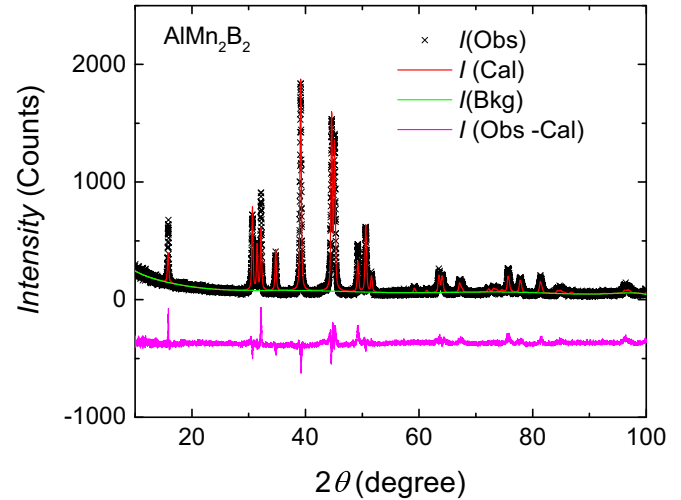
FIG. 3. Single crystal crushed powder XRD pattern where *I* (Obs), *I*(Cal), *I*(Bkg), and *I*(Obs-Cal) are observed, calculated, background, and differential diffractrograms, respectively.

Research, Inc. ac (1 mA, 17 Hz) resistance bridge (LR 700). Thin platinum wires were attached to the sample using DuPont 4929N silver paint to make electrical contact. Quantum Design magnetic property measurement system (MPMS) was used as a temperature controller. The measured temperature dependent electrical resistance of $AlMn_2B_2$ is shown in Fig. 5. These data further confirm that our single crystals are essentially stoichiometric $AlMn_2B_2$; given that the residual resistivity ratio ($\frac{R(350.0K)}{R(2.0K)}$) is 28.5, there is relatively low disorder scattering. In addition, a very clear feature is seen in both R(T) and $\frac{d(R(T))}{dT}$ at $T = 313 \pm 2$ K. Such features are often related to a loss of spin disorder
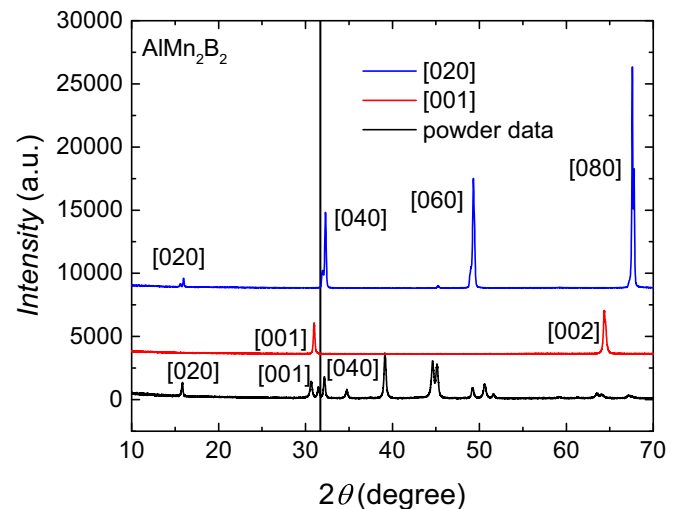
FIG. 4. Crystallographic orientation characterization of $AlMn_2B_2$ surfaces using monochromatic Cu K_α radiation in Bragg Brentano diffraction geometry. The top curve shows the family of [020] peaks identifying the direction perpendicular to the plate as [010]. The direction along the thickness of the plates is found to be [001] leaving the direction along the length as [100]. The vertical grid line through the [110] powder diffraction peak (not labeled in diagram) is a reference to identify [001] and [040] peaks observed for different facets.
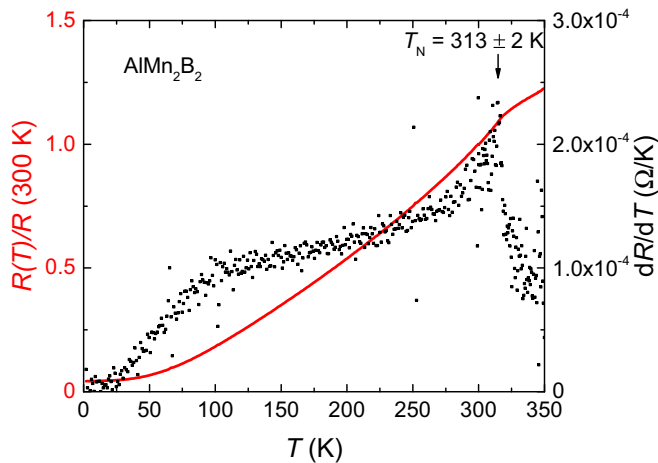
FIG. 5. Temperature dependent normalized resistance (left axis) and temperature derivative (right axis) of $AlMn_2B_2$. The resistance is metallic in nature. The temperature derivative shows an anomaly at 313 ± 2 K consistent with an AFM phase transition.

scattering at a magnetic transition [18]. As such, these data are our first suggestion that $AlMn_2B_2$ may indeed have some form of magnetic order below 315 K.

The magnetic properties of $AlMn_2B_2$ were studied from a base temperature of 2 K to 700 K. Low temperature anisotropic magnetization data of single crystalline $AlMn_2B_2$ samples were measured within the temperature range 2–350 K using a MPMS. High temperature, anisotropic temperature dependent magnetization data were obtained using a Quantum Design VersaLab vibrating sample magnetometer (VSM) over the temperature range 300–700 K in an oven option mode.

The low temperature anisotropic susceptibility data, with $H = 3$ T applied field, are presented in Fig. 6. Below 50 K, the magnetization data show a low temperature upturn as reported in previous literature [5]. In all three directions, there is a clear anomaly in susceptibility data around 312 K. The inset
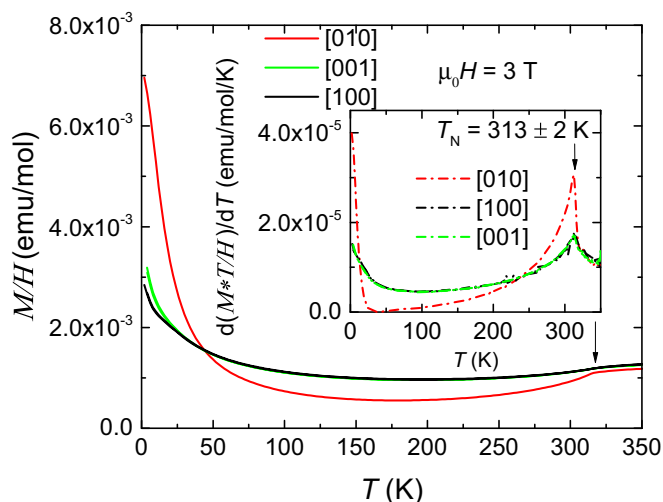

FIG. 6. Low temperature (2–350 K) M/H along various crystallographic axes of $AlMn_2B_2$ sample as outlined in the graph. The inset shows $\frac{d(M*T/H)}{dT}$ as a function of temperature.
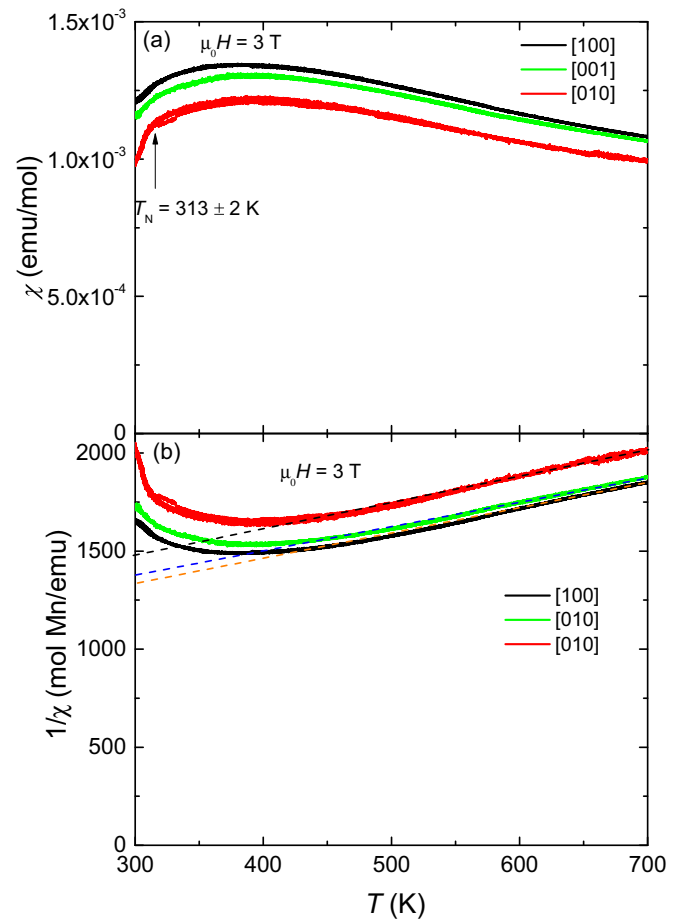

FIG. 7. (a) High temperature susceptibility data along various axes measured using VSM. There are shallow anomalies present around 313 ± 2 K for each direction. (b) Corresponding Curie Weiss plots identifying $AlMn_2B_2$ as an AFM material with $\theta_{010} = -815$ K, $\theta_{100} = -750$ K, and $\theta_{001} = -835$ K, respectively.

shows $\frac{d(M*T/H)}{dT}$ as a function of temperature [19] showing a clear anomaly around 312 K identifying $AlMn_2B_2$ as an AFM material. The observed anomaly in $\frac{d(M*T/H)}{dT}$ coincides with the kink observed in $\frac{dR}{dT}$.

Recently, $AlMn_2B_2$ was reported to be AFM however Neel temperature was reported to be around 390 K [7]. To examine higher temperatures, our high temperature susceptibility data, obtained using our VSM, are presented in Figs. 7(a) and 7(b). Although a broad local maximum of the susceptibility around 350–390 K for different axes consistent to Ref. [7] was found, the $\frac{d(M*T/H)}{dT}$ did not show any anomaly. The only clear and conclusive feature in the high temperature data associated with a magnetic transition is the feature at 313 ± 2 K. The broad local maximum in magnetization well above the transition temperature can be associated with low-dimensional or linear chain anisotropic Heisenberg antiferromagnetism [20–24]. The fitted Curie Weiss temperatures for various axes were obtained to be $\theta_{010} = -815$ K, $\theta_{100} = -750$ K, and $\theta_{001} = -835$ K. From the average slope of Curie Weiss plot, the effective moment of Mn is found to be ~2.5 μ_B/Mn.

At low temperature, $T \leqslant 50$ K, in Fig. 6 there is a clear upturn in the M/H data, particularly for H along the [010]
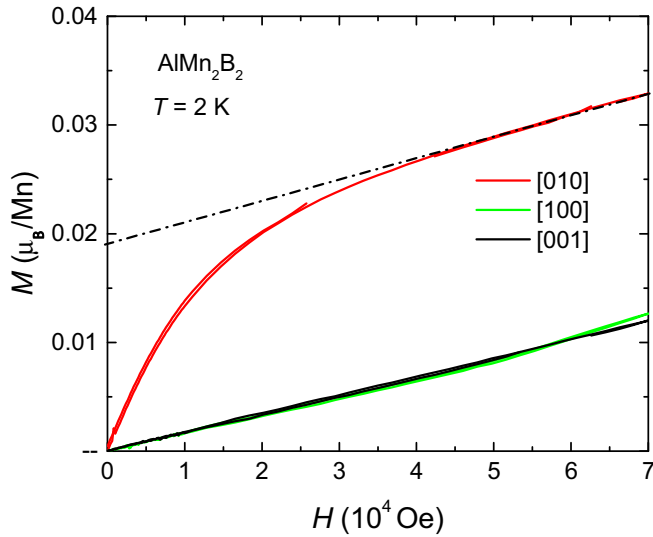
FIG. 8. Field dependent magnetization $M(H)$ of AlMn$_2$B$_2$ at 2 K. The magnetization along the [010] direction shows a saturation magnetization of 0.02 μ_B/Mn with respect to the other two principle directions outlined with a linear fit of the high field region data. The $M(H)$ data along the [010] direction shows no magnetic hysteresis, i.e., the almost overlapping two red curves for increasing and decreasing field. At higher field region, all three $M(H)$ data have the same slopes.

direction. In order to better understand this we measured the anisotropic field dependent magnetization at 2 K as shown in Fig. 8. For fields greater than 4 T the slopes of the $M(H)$ plots are comparable for all three directions. For $H \parallel$ [010], there is a roughly 0.02 μ_B/Mn offset due to Brillouin function type magnetization for $\mu_0 H \leqslant 3$ T. The origin of this small, anisotropic contribution is currently not known.

V. NUCLEAR MAGNETIC RESONANCE STUDY

To further investigate the magnetism of AlMn$_2$B$_2$, we carried out ^{11}B-NMR measurements at various temperatures between 5 K and 430 K as presented in Figs. 9–11. To perform the NMR measurements for the temperature region of $T =$ 5–295 K, crushed single crystalline powder was enclosed in a weighing paper folded closed cylindrical tube and inserted inside the NMR coil. For the higher temperature NMR measurements up to 430 K from room temperature, the crushed powder was sealed under $\frac{1}{3}$ atmospheric pressure of Ar inside a ~1 mm internal diameter amorphous silica tube. The NMR measurements were carried out using a laboratory-built phase coherent spin-echo pulsed NMR spectrometer on ^{11}B (nuclear spin $I = \frac{3}{2}$ and gyromagnetic ratio $\frac{\gamma_N}{2\pi} = 13.6552$ MHz/T) nuclei in the temperature range $5 < T < 430$ K. NMR spectra were obtained either by Fourier transform of the NMR echo signals, by sweeping frequency or by sweeping magnetic field. Magnetic phase transition was studied analyzing the full width at half maximum (*FWHM*) of ^{11}B-NMR spectra and
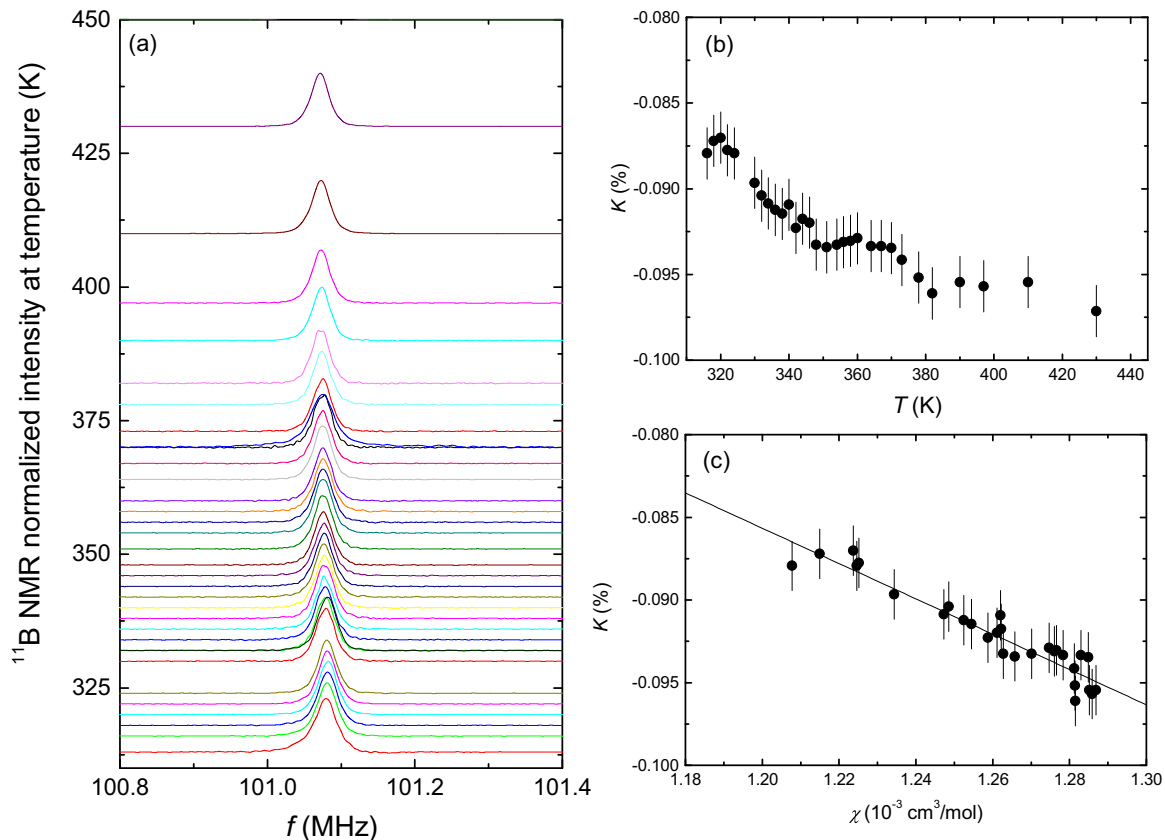

FIG. 9. ^{11}B-NMR spectra (a) and their Knight shifts (b) measured at different temperatures from 315 to 430 K with $H = 7.4089$ T. (c) Knight shift as a function of susceptibility with temperature as an implicit parameter where the black line shows a linear fit.
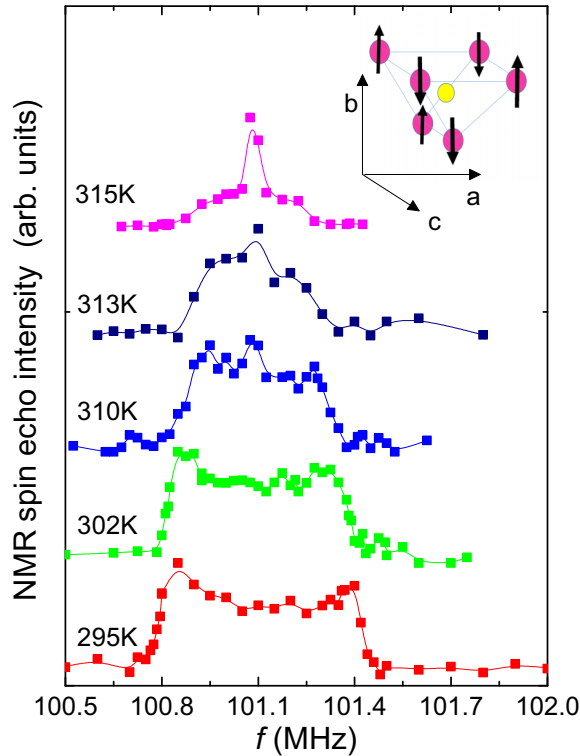
FIG. 10. ^{11}B-NMR spectra measured at $H = 7.4089$ T by sweeping frequency. Inset shows the six nearest Mn neighbors of B with a possible antiferromagnetic spin orientation [7].

spin-lattice relaxation rate $\frac{1}{T_1}$. The ^{11}B $\frac{1}{T_1}$ was measured by the conventional single saturation pulse method.

Figure 9(a) shows the ^{11}B-NMR spectra obtained by Fourier transform of the NMR spin echo for temperatures in the range 315–430 K at $H = 7.4089$ T. Throughout the range of study, the *FWHM* ~29 kHz is nearly independent of temperature. Figure 9(b) shows the temperature dependence of the NMR shift (K) in the paramagnetic state, where K decreases with increasing T. The temperature dependence of K follows that of χ as shown in Fig. 9(c) where K is plotted as a function of χ with temperature as an implicit parameter. From the slope of the K-χ plot, the hyperfine coupling constant A_{hf} is estimated to be 12 kOe/μ_B using the relation of $K = A_{hf}\,\chi/\mu_B N_A$ where N_A is the Avogadro number. The total hyperfine coupling constant at the B site is generally the sum of the transferred hyperfine (A_{trans}) and dipolar (A_{dip}) couplings produced by the Mn spins: $A_{hf} = zA_{trans} + A_{dip}$ where $z = 6$ is the number of nearest neighbor Mn spins with respect to the B site. The dipolar coupling was calculated to be at most 1 kOe/μ_B which is one order of magnitude smaller than the total hyperfine field. This suggests that the dominant contribution of the total hyperfine coupling is due to the transferred hyperfine coupling at the B site. Below 315 K, as shown in Fig. 10, the ^{11}B-NMR line broadens abruptly and has an almost rectangular shape at low temperatures. Since the rectangular shape is characteristic of the NMR spectrum in the AFM ordered state for the powder sample, the results clearly indicate that the magnetic phase transition around 315 K is AFM. Similar rectangular NMR spectra in the AFM state have
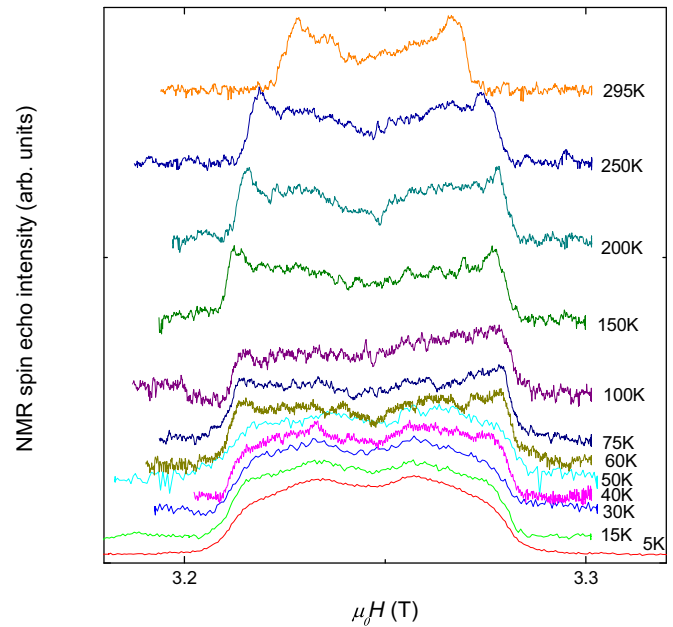

FIG. 11. ^{11}B-NMR spectra measured at different temperatures between 5 K and 295 K measured using field sweeping method. A noticeable change in shape of ^{11}B-NMR peaks around 50 K coincides with changing the magnetic anisotropy between [100]/[001] and [010] directions as shown in Fig. 6.

been observed in $BiMn_2PO_6$ [25], $NaVGe_2O_6$ [26], CuV_2O_6 [27], and $BaCo_2V_2O_8$ [28].

In the low temperature range between 5–295 K, several ^{11}B-NMR spectra were measured at a frequency of $f = 44.32$ MHz by sweeping the magnetic field as shown in Fig. 11. The *FWHM* increases with decreasing temperature and shows nearly constant (~0.07 T) down to ~50 K. Below 50 K, the *FWHM* slightly decreases, where the shape of the spectrum changes and the edges of the lines are smeared out. These results suggest a change in magnetic state around 50 K. Although it is not clear at present, it is interesting if the change relates to the strong enhancement of χ_b below 50 K as shown in Fig. 6. NMR measurements on single crystals could provide additional information in this issue. This is for future work.

Figure 12(a) shows the temperature variation of the *FWHM* of the ^{11}B-NMR spectra between 5–430 K. Since the *FWHM* of the powder NMR spectrum in the AFM state corresponds to twice the internal field (H_{int}) at the B site produced by Mn ordered moments [25–29], the temperature dependence of *FWHM* reflects the temperature dependence of the Mn sublattice magnetization. Therefore, one can obtain the critical exponent (β) of the order parameter using the formula $FWHM \propto (1 - \frac{T}{T_N})^\beta$. The maximum value of $\beta = 0.21 \pm 0.02$ with $T_N = 314$ K was obtained by fitting the data points in the range 295–315 K close to T_N as shown in Fig. 12(b). Very nominal change was observed in the fitted β parameter with the extension of fitted range toward the low temperature. The observed change in critical exponent β was within the error bar for all the temperature range. These power law fittings of *FWHM* provided a lower value of $\beta = 0.21 \pm 0.02$ (for 3D Heisenberg model $\beta \sim 0.345$) suggesting a low-dimensional magnetism as discussed in Ref. [20].
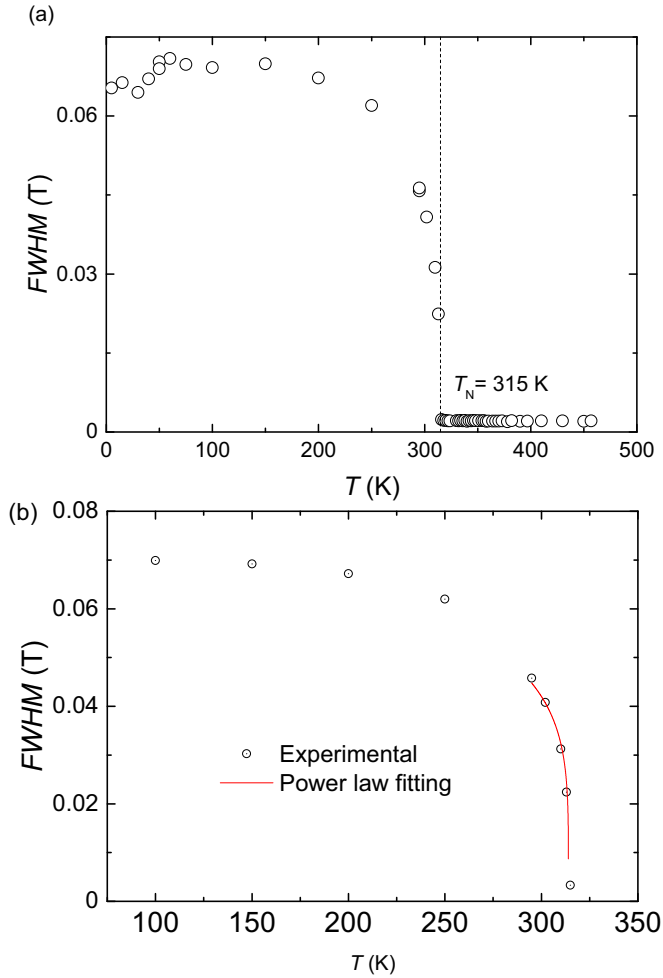
(a)

(b)

FIG. 12. (a) Temperature dependence of *FWHM* ^{11}B-NMR spectra in powdered $AlMn_2B_2$ sample showing AFM transition around 315 K. (b) Power law fitting of the observed temperature variation of ^{11}B *FWHM* in the temperature range 295–315 K as $FWHM \propto [1 - (\frac{T}{T_N})]^\beta$ with $T_N = 314$ K and $\beta = 0.21 \pm 0.02$.

In general, one may be able to estimate an ordered magnetic moment in the magnetically ordered state if the hyperfine coupling constant and the internal field were known. However, in antiferromagnetic states, the estimation of the ordered magnetic moment is not straightforward due to a cancellation of hyperfine fields. Taking the spin structure from the neutron diffraction measurements [7] shown in the inset of Fig. 10 into consideration, a small internal field at the B site is expected due to the cancellation of the transferred hyperfine fields produced by the six nearest neighbor Mn ions in $AlMn_2B_2$. In fact, using the observed internal field ($|H_{int}| \sim 0.35$ kOe) and the total hyperfine coupling constant of -12 kOe/μ_B, the ordered moment is estimated to be 0.03 μ_B which is much smaller than the reported value of $0.71/\mu_B$, evidencing the cancellation of the hyperfine field at the B site in the antiferromagnetic state. If we assume that the transferred hyperfine field at the B site from each Mn ion is the same for the six nearest neighbor Mn ions, zero internal field is expected due to a perfect cancellation. The observed small H_{int} could originate from a nonperfect cancellation of
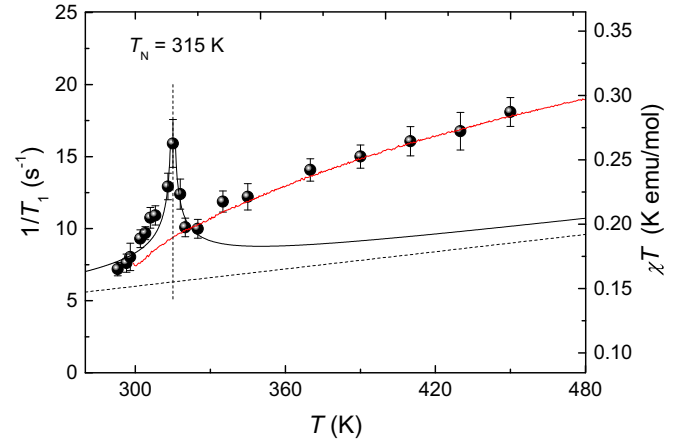

FIG. 13. The relaxation rate ($\frac{1}{T_1}$) is plotted as a function of T from 293 K to 450 K. The transition temperature at 315 K is evidenced by a sharp peak of $\frac{1}{T_1}$. The black line is the best fit with a weak itinerant antiferromagnet model: ($\frac{1}{T_1} = \frac{0.03T}{|(T-T_N)|^{1/2}} + 0.02T$). The red line shows the temperature dependence of χT. The black dotted line exhibits the contribution of the Korringa-type relation ($\frac{1}{T_1} = 0.02T$) to the weak antiferromagnet model.

the hyperfine field due to the orthorhombic symmetry where the assumption of the uniform hyperfine field from the six Mn spins is slightly broken down, making the analysis more complicated. The dipolar field may also contribute to the small internal field in the antiferromagnetic state. Further detailed analysis is required to estimate the ordered magnetic moment in $AlMn_2B_2$ using the NMR data, which is beyond the scope of the present manuscript.

To study the dynamical properties of the Mn spins in high temperature range, the spin lattice relaxation rates ($\frac{1}{T_1}$) at the ^{11}B site were measured from room temperature to 430 K. Figure 13 shows the temperature dependence of $\frac{1}{T_1}$ where $\frac{1}{T_1}$ shows a clear peak at 315 K, evidencing again the AFM ordering. On the other hand, no clear anomaly in the temperature dependence of $\frac{1}{T_1}$ is observed around 390 K where the magnetic susceptibility exhibits a broad local maximum. Therefore, the broad maximum in the magnetic susceptibility is not associated with a magnetic ordering, but it could be attributed to a two-dimensional magnetic character in $AlMn_2B_2$ as observed in 2D AFM compounds such as $BaMn_2Si_2O_7$ [20].

Finally it is interesting to discuss the nature of the magnetic fluctuations in $AlMn_2B_2$ based on the T_1 data. Since the ordered magnetic moment in the antiferromagnetic state is reported to be 0.71 μ_B [7], the compound could be regarded as a weak itinerant antiferromagnet. According to self-consistent renormalization theory [30], $\frac{1}{T_1}$ for weak itinerant antiferromagnets is described as $\frac{1}{T_1} = \frac{aT}{|(T-T_N)|^{1/2}} + bT$ where the first term originates from antiferromagnetic fluctuations around a wave vector $q = Q$ (Q being antiferromagnetic wave vector) and the second term is due to Korringa-type relaxation, a characteristic feature of metallic materials [31]. As shown by the black line in Fig. 13, although the equation with $a = 0.03$ ($s^{-1} K^{-0.5}$) and $b = 0.02$ ($s^{-1} K^{-1}$) seems to reproduce the data close to T_N, the temperature dependence of $\frac{1}{T_1}$ above

$T \sim 325$ K cannot be well reproduced. Instead, we found the temperature dependence of $\frac{1}{T_1}$ above 325 K is well reproduced by the temperature dependence of χT shown by the red line in Fig. 13. Such a behavior of $\frac{1}{T_1} \sim \chi T$ has been observed in many antiferromagnetic insulators with local moments such as $Pb_2VO(PO_4)_2$ [32], $VOMoO_4$ [33], and $BiMn_2PO_6$ [25]. These results suggest that the magnetic fluctuations in the paramagnetic state of $AlMn_2B_2$ are dominated by the uniform paramagnetic fluctuations, similar to the localized spin systems. Further experiments are required to characterize the magnetic fluctuations in the AFM state well below T_N, which will be a future project.

VI. CONCLUSIONS

Structural, electrical transport, and magnetic properties were studied on self flux grown single crystalline $AlMn_2B_2$ samples. All these measurements revealed $AlMn_2B_2$ as an AFM compound with a transition temperature around 313 ± 2 K. At higher temperature a broad hump, well above the transition temperature, could be the signature of low-dimensional magnetic interaction in $AlMn_2B_2$ above the room temperature.

[1] Q. Du, G. Chen, W. Yang, J. Wei, M. Hua, H. Du, C. Wang, S. Liu, J. Han, Y. Zhang, and J. Yang, Magnetic frustration and magnetocaloric effect in $AlFe_{2-x}Mn_xB_2$(x = 0–0.5) ribbons, J. Phys. D: Appl. Phys. **48**, 335001 (2015).

[2] X. Tan, P. Chai, C. M. Thompson, and M. Shatruk, Magnetocaloric effect in $AlFe_2B_2$: Toward magnetic refrigerants from earth-abundant elements, J. Am. Chem. Soc. **135**, 9553 (2013).

[3] T. N. Lamichhane, L. Xiang, Q. Lin, T. Pandey, D. S. Parker, T.-H. Kim, L. Zhou, M. J. Kramer, S. L. Bud'ko, and P. C. Canfield, Magnetic properties of single crystalline itinerant ferromagnet $AlFe_2B_2$, Phys. Rev. Materials **2**, 084408 (2018).

[4] R. Barua, B.T. Lejeune, L. Ke, G. Hadjipanayis, E. M. Levin, R. W. McCallum, M. J. Kramer, and L. H. Lewis, Anisotropic magnetocaloric response in $AlFe_2B_2$, J. Alloys Compd. **745**, 505 (2018).

[5] P. Chai, S. A. Stoian, X. Tan, P. A. Dube, and M. Shatruk, Investigation of magnetic properties and electronic structure of layered-structure borides AlT_2B_2 (T=Fe, Mn, Cr) and $AlFe_{2-x}Mn_xB_2$, J. Solid State Chem. **224**, 52 (2015).

[6] L. Ke, B. N. Harmon, and M. J. Kramer, Electronic structure and magnetic properties in T_2AlB_2 (T = Fe, Mn, Cr, Co, and Ni) and their alloys, Phys. Rev. B **95**, 104427 (2017).

[7] D. Potashnikov, E. N. Caspi, A. Pesach, A. Hoser, S. Kota, L. Verger, M. W. Barsoum, I. Felner, A. Keren, and O. Rivin, Magnetic ordering in the nano-laminar ternary Mn_2AlB_2 using neutron and X-ray diffraction, J. Magn. Magn. Mater. **471**, 468 (2019).

[8] L. Verger, S. Kota, H. Roussel, T. Ouisse, and M. W. Barsoum, Anisotropic thermal expansions of select layered ternary transition metal borides: MoAlB, Cr_2AlB_2, Mn_2AlB_2, and Fe_2AlB_2, J. Appl. Phys. **124**, 205108 (2018).

[9] K. D. Belashchenko, L. Ke, M. Dane, L. X. Benedict, T. N. Lamichhane, V. Taufour, A. Jesche, S. L. Bud'ko, P. C. Canfield, and V. P. Antropov, Origin of the spin reorientation transitions in $(Fe_{1-x}Co_x)_2B$ alloys, Appl. Phys. Lett. **106**, 062408 (2015).

[10] P. C. Canfield and I. R. Fisher, High-temperature solution growth of intermetallic single crystals and quasicrystals, J. Cryst. Growth **225**, 155 (2001).

[11] W. R. Meier, T. Kong, S. L. Bud'ko, and P. C. Canfield, Optimization of the crystal growth of the superconductor $CaKFe_4As_4$ from solution in the FeAs - $CaFe_2As_2$ - KFe_2As_2 system, Phys. Rev. Materials **1**, 013401 (2017).

[12] Paul C. Canfield, T. Kong, U. S. Kaluarachchi, and N. H. Jo, Use of frit-disc crucibles for routine and exploratory solution growth of single crystalline samples, Philos. Mag. **96**, 84 (2016).

[13] T. N. Lamichhane, V. Taufour, M. W. Masters, D. S. Parker, U. S. Kaluarachchi, S. Thimmaiah, S. L. Bud'ko, and P. C. Canfield, Discovery of ferromagnetism with large magnetic anisotropy in ZrMnP and HfMnP, Appl. Phys. Lett. **109**, 092402 (2016).

[14] SHELXTL-v2008/4, Bruker AXS Inc., Madison, Wisconsin, USA, 2013.

[15] A. C. Larson and R. B. Von Dreele, General structure analysis system, Los Alamos National Laboratory Report No. LAUR 86-748 (2004).

[16] B. H. Toby, *EXPGUI*, a graphical user interface for *GSAS*, J. Appl. Crystallogr. **34**, 210 (2001).

[17] A. Jesche, M. Fix, A. Kreyssig, W. R. Meier, and P. C. Canfield, X-ray diffraction on large single crystals using a powder diffractometer, Philos. Mag. **96**, 2115 (2016).

[18] M. E. Fisher and J. S. Langer, Resistive Anomalies at Magnetic Critical Points, Phys. Rev. Lett. **20**, 665 (1968).

[19] M. E. Fisher, Relation between the specific heat and susceptibility of an antiferromagnet, Philos. Mag. (1798-1977) **7**, 1731 (1962).

[20] J. Ma, C. D. Dela Cruz, T. Hong, W. Tian, A. A. Aczel, S. Chi, J.-Q. Yan, Z. L. Dun, H. D. Zhou, and M. Matsuda, Magnetic phase transition in the low-dimensional compound $BaMn_2Si_2O_7$, Phys. Rev. B **88**, 144405 (2013).

[21] A. N Vasil'ev, L. A Ponomarenko, H. Manaka, I. Yamada, M. Isobe, and Y. Ueda, Quasi-one-dimensional antiferromagnetic spinel compound $LiCuVO_4$, Physica B: Condensed Matter **284–288**, 1619 (2000).

[22] Y. J. Kim, M. Greven, U.-J. Wiese, and R. J. Birgeneau, Monte-carlo study of correlations in quantum spin chains at non-zero temperature, Eur. Phys. J. B **4**, 291 (1998).

[23] J. C. Bonner and M. E. Fisher, Linear magnetic chains with anisotropic coupling, Phys. Rev. **135**, A640 (1964).

[24] R. Dingle, M. E. Lines, and S. L. Holt, Linear-Chain Antiferromagnetism in $[(CH_3)_4N][MnCl_3]$, Phys. Rev. **187**, 643 (1969).

[25] R. Nath, K. M. Ranjith, B. Roy, D. C. Johnston, Y. Furukawa, and A. A. Tsirlin, Magnetic transitions in the spin-$\frac{5}{2}$ frustrated magnet $BiMn_2PO_6$ and strong lattice softening in $BiMn_2PO_6$ and $BiZn_2PO_6$ below 200 K, Phys. Rev. B **90**, 024431 (2014).

[26] B. Pedrini, J. L. Gavilano, D. Rau, H. R. Ott, S. M. Kazakov, J. Karpinski, and S. Wessel, NMR and dc susceptibility studies of $NaVGe_2O_6$, Phys. Rev. B **70**, 024421 (2004).

[27] J. Kikuchi, K. Ishiguchi, K. Motoya, M. Itoh, K. Inari, N. Eguchi, and J. Akimitsu, NMR and neutron scattering studies of quasi one-dimensional magnet CuV_2O_6, J. Phys. Soc. Jpn. **69**, 2660 (2000).

[28] Y. Ideta, Y. Kawasaki, Y. Kishimoto, T. Ohno, Y. Michihiro, Z. He, Y. Ueda, and M. Itoh, ^{51}V NMR study of antiferromagnetic state and spin dynamics in quasi-one-dimensional $BaCo_2V_2O_8$, Phys. Rev. B **86**, 094433 (2012).

[29] A. Yogi, N. Ahmed, R. Nath, A. A. Tsirlin, S. Kundu, A. V. Mahajan, J. Sichelschmidt, B. Roy, and Y. Furukawa, Antiferromagnetism of $Zn_2VO(PO_4)_2$ and the dilution with Ti^{4+}, Phys. Rev. B **91**, 024413 (2015).

[30] T. Moriya and K. Ueda, Nuclear magnetic relaxation in weakly ferro- and antiferromagnetic metals, Solid State Commun. **15**, 169 (1974).

[31] Y. Kitaoka and H. Yasuoka, NMR investigations on the spin fluctuations in itinerant antiferromagnets. I. V_3Se_4 and V_5Se_8, J. Phys. Soc. Jpn. **48**, 1460 (1980).

[32] R. Nath, Y. Furukawa, F. Borsa, E. E. Kaul, M. Baenitz, C. Geibel, and D. C. Johnston, Single-crystal ^{31}P NMR studies of the frustrated square-lattice compound $Pb_2(VO)(PO_4)_2$, Phys. Rev. B **80**, 214430 (2009).

[33] P. Carretta, N. Papinutto, C. B. Azzoni, M. C. Mozzati, E. Pavarini, S. Gonthier, and P. Millet, Frustration-driven structural distortion in $VOMoO_4$, Phys. Rev. B **66**, 094420 (2002).